Automatic procedure for evaluating the Paris Law of martensitic and austenitic stainless steels by means of thermal methods

Accepted Manuscript

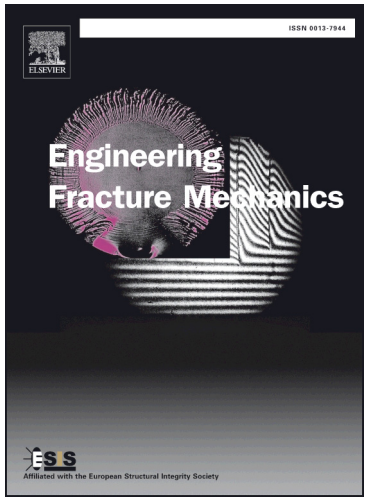

Automatic procedure for evaluating the Paris Law of martensitic and austenitic stainless steels by means of thermal methods

F. Ancona, D. Palumbo, R. De Finis, G.P. Demelio, U. Galietti

PII: S0013-7944(16)30272-7
DOI: http://dx.doi.org/10.1016/j.engfracmech.2016.06.016
Reference: EFM 5231

To appear in: *Engineering Fracture Mechanics*

Received Date: 4 March 2016
Revised Date: 20 June 2016
Accepted Date: 22 June 2016

Please cite this article as: Ancona, F., Palumbo, D., De Finis, R., Demelio, G.P., Galietti, U., Automatic procedure for evaluating the Paris Law of martensitic and austenitic stainless steels by means of thermal methods, *Engineering Fracture Mechanics* (2016), doi: http://dx.doi.org/10.1016/j.engfracmech.2016.06.016

Automatic procedure for evaluating the Paris Law of martensitic and austenitic stainless steels by means of thermal methods

F. Ancona, D. Palumbo, R. De Finis, G.P. Demelio, U. Galietti

Department of Mechanics, Mathematics and Management (DMMM), Politecnico di Bari, Viale Japigia 182, 70126, Bari, Italy

Abstract

Determination of the Paris Law constants implies the knowledge of both Stress Intensity Factor (SIF) and the crack growth rate (*da/dN*). In this regard, the crack length and the SIF values can be measured using various methods suggested by literature and proposed by Standards, but most of them require an off-line measurement of the crack with consequent high testing time and cannot be applied on actual structural components.

In this work, the Thermoelastic Stress Analysis (TSA) technique is used for the monitoring of fatigue crack growth during fracture mechanics tests on four stainless steels: AISI 422 and ASTM A182 grade F6NM with martensitic lattice and CF3M and CF8M with austenitic lattice. In particular, an automatic procedure based on the TSA technique was proposed for the continuous evaluation of the crack tip position and the SIF value. Advantages with respect to classical methods can be obtained in terms of reduction of: testing time, experimental set-up, data processing and data report.

Keywords: austenitic steels, martensitic steel, thermoelastic stress analysis (TSA), crack growth rate, Paris Law.

1. Introduction

Paris's Law describes the behaviour of cracked materials subjected to dynamic loading and it implies the knowledge of both the stress intensity factor (SIF) and the crack growth rate (*da/dN*) [1], [2]. In this regard, these parameters can be obtained by use of conventional methods according to Standards [3], by means of experimental and non-destructive techniques [4-21]. In particular, the most widely diffused methods used for the monitoring and the measurement of crack growth rate are microscopy, extensometry, ultrasound, X-ray and DIC (Digital Image Correlation) [3], [4-10].

Saka *et al.*, [5] proposed a non-destructive method for evaluating a 3D surface crack based on a magnetic field induced in the air by DC current flow in materials. This method requires two probes for application of the DC current and cracks have to be extremely small in comparison with the distance between the probes. A 3D X-ray synchrotron tomography was used by Williams *et al.*, [6] to obtain local measurements of crack growth in a 7075-T6 aluminium alloy. This instrumentation allows for in situ measurements of crack opening displacement (COD) but requires a suited precision alignment fixture for *in situ* testing.

In Kainuma's work [7], a quantitative examination of the efficiency of micro-encapsulated dye mixing paint was performed. This method allows for an easily applicable inspection also on actual

structural components. However, it presents difficulty when detecting initial crack and short fatigue crack. The magnetic flux density around the fatigue crack was observed in the work of Tanabe *et al.*, [8].The magnetic flux was measured by means of a Magneto-Impedance sensor and a strong correlation was found with the stress intensity factor. However, this technique does not allow for an accurate crack length measurement.

Infrared thermography (IRT) was also proposed for the study of the fracture behaviour of materials subjected to fatigue loading [11-21]. In particular, a temperature rise due to the heat dissipations can be observed around the crack tip where the plastic zone is located. In this regard, Carrascal *et al.*, [11] used IRT for evaluating the Paris Law constants of a polymer (polyamide) with an experimental methodology. A good agreement was found with respect to traditional calculation methods. However, this procedure may find limitation in those cases in which temperature changes on material related to the plastic zone are very low (short cracks) and, moreover, high performance equipment and a difficult set-up are required. This is the case, for instance, with brittle materials (such as martensitic steels), welded joints and aluminium alloys [22-25].

The aims of this work are: to propose an automatic procedure based on the Thermoelastic Stress Analysis (TSA) technique, to assess the Paris Law constants and to study, with the proposed procedure, the fracture behaviour of 4 stainless steels for which there is a lack of data present in literature.

Thermoelastic Stress Analysis (TSA), based on the thermoelastic effect, is a non-contact, full field technique that provides stress maps of a component subjected to dynamic loading [26-33]. In adiabatic and linear elastic conditions, a solid body subjected to a load undergoes a change of temperature proportional to the first stress invariant.

TSA technique can be used for the determination of the stress intensity factor during fracture mechanics tests [14-21]. By knowing the sum of the principal stresses, it is possible to determine the stress intensity factor and, at the same time, it is possible to determine the crack growth rate by analyzing the phase data [14-21]. In particular, Tomlinson *et al*. [14], [15] demonstrated the potential of TSA by using the amplitude of the thermoelastic signal for the crack tip and the SIF evaluation. In the works of Diaz *et al.,* [16-19] the phase signal was proposed for detecting the crack tip position. In fact, phase changes of the signal are due to high stress gradients which may be ascribed to the non-adiabatic conditions and to the plastic behaviour of the crack tip. The characteristic performance of the phase signal at the crack tip contains a double reversal of sign, notably caused by the two cited effects which have the opposite sign influence [16-19]. In literature, phase signal is also considered as an effective parameter for the identification of local damage and for the evaluation of fatigue damage in materials [22-25].

This paper presents an automatable experimental procedure to characterize the fracture behaviour of steels and represents the completion of the works [20], [21].

Four stainless steels were tested: AISI 422 and ASTM A182 grade F6NM with martensitic lattice and CF3M and CF8M with austenitic lattice. These steels are used in engineering fields where resistance to high temperatures, corrosive environments and high mechanical stress are required [34], [35]. However, despite their wide use in engineering, there is for these materials, a lack of information in literature about their fatigue and fracture behaviour.

Three CT steel specimens were used and tested according to ASTM E 647-00 for each material and the monitoring of crack tip growth was performed in a continuous manner by means of a cooled IR camera. The analysis of thermographic data provides the Paris Law constants. Finally, a comparison with conventional methods was performed.

The proposed procedure allows for the on-line monitoring of crack growth during testing through a set-up which is simple compared to other techniques. Moreover, a simple specimen preparation is required, which makes the proposed procedure also suitable for the monitoring of actual structural components.

2. Theory

The thermoelastic effect was reported for the first time in the work of Lord Kelvin and describes the reversible variation in temperature that occurs in a solid when it is deformed in the elastic range [27], [29]. This effect depends on the variation in volume during the deformation of the solid. In solids, the temperature change appears to be of the order of milliKelvin and under adiabatic and reversible conditions, the temperature variations expected are proportional to the sum of principal stresses. The relation between the change in temperature due to the application of loading and the stress range of a linear elastic and homogeneous material can be written as:

$$\Delta T = - KT_0\Delta(c_1 + c_2) \tag{1}$$

where $K=\alpha/\rho Cp$ is the thermoelastic constant of the material, α is the coefficient of thermal expansion, Cp is the specific heat at constant pressure, ρ is the density, T_0 is the initial temperature and $\Delta(\sigma_1+ \sigma_2)$ the sum of the principal stresses [27], [29]. The infrared detector of the thermocamera is able to detect the infrared flux emitted from the surface of the stressed body and it produces a signal S related to the sum of the principal stresses.

$$SA = \Delta c \tag{2}$$

where A is the calibration factor depending on: material, type of instrument used and environmental conditions of the test. Calibration of thermoelastic signal is needed to determine A and then to evaluate $\Delta\sigma$ and it is usually performed by means of three different approaches [29], [33].
More detailed description about the use of TSA for cracked components will be provided in the following sections.

3. Experimental set-up

3.1 Specimen geometry and materials

Four stainless steels were used in this work, AISI 422 and ASTM A182 grade F6NM with martensitic lattice, CF3M and CF8M with austenitic lattice. Martensitic stainless steels have a higher mechanical strength obtained by a quenching heat treatment compared with austenitic steels; the corrosion resistance is higher in austenitic stainless steel due to the higher percentage of chromium. In Tables 1 and 2, the chemical composition and the mechanical properties of the stainless steel tested in this work are presented [35].

Table 1**:** Chemical composition of stainless steels tested in the work

Materials [%]	**C**	**P**	**Si**	**Ni**	**V**	**Mn**	**Cr**	**S**	**Mo**	**W**
AISI 422	0.20-0.25	0.025	0.4	0.50-1.00	0.15-0.30	1.0	11.0-13.0	0.025	0.75-1.25	0.75-1.25
ASTM A182 grade F6NM	0.15	0.040	1.0	3.50-5.50	-	1.0	11.5-13.5	0.070	0.50-1.00	-
CF3M	0.03	0.015	1.0	10.0-14.0	-	2.0	10.0-18.0	0.030	2.00-3.00	-
CF8M	0.08	0.015	1.0	10.0-14.0	-	2.0	14.0-18.0	0.030	2.00-3.00	-

Table 2: Mechanical properties (at room temperature) of stainless steels tested in the work

Materials	**E** [MPa]	σ_y[MPa]	σ_{UTS}[MPa]
AISI 422	200,000	760.2	965.8
ASTM A182 grade F6NM	198,500	615.7	911.6
CF3M	200,000	275.8	586.0
CF8M	200,000	275.2	551.2

Three Compact Tension (CT) specimens were used with dimensions according to ASTM E 647 [3] for each material tested. In Figure 1, dimensions of the specimen are reported in mm. Specimens were sprayed with flat black spray to increase the emissivity to 0.95.

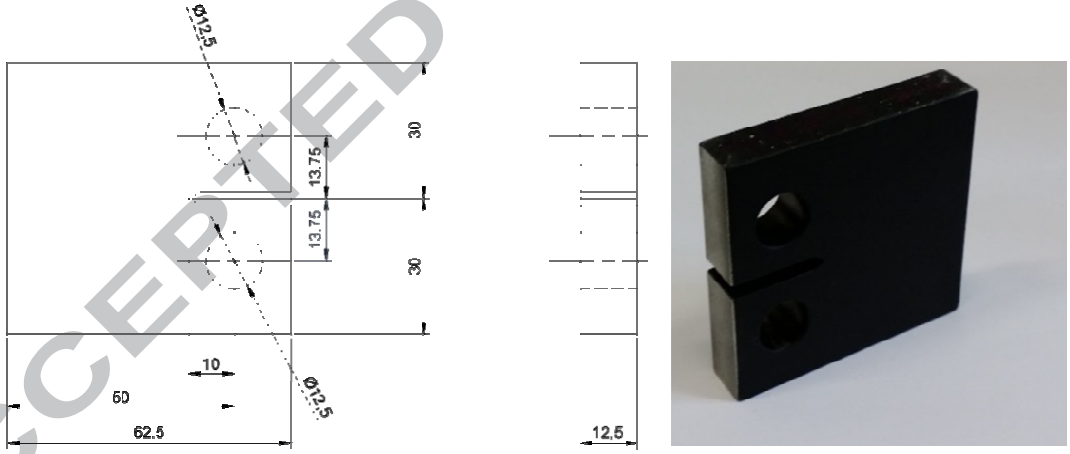

Figure 1. Specimen dimension in mm according to ASTM E 647-00.

3.2 Testing procedure

The tests were carried out with the MTS model 370 servo hydraulic fatigue machine with a 100 kN capacity. According to ASTM E 647 [3] the constant-force-amplitude procedure was used with a constant force range ΔP, fixed stress ratio ($R=0.1$) and loading frequency f=13 Hz. In Table 3, the loading ranges used during the tests for each material are reported.

Table 3: Loading amplitude used for all materials.

Material	**ΔP** [kN]
AISI 422	10.8
ASTM A 182 grade F6NM	12.4
CF3M	9.90
CF8M	9.45

Thermographic sequences were acquired with constant intervals of 2000 cycles by using a cooled FLIR IR X6540 SC infrared camera with an InSb detector (640x512 pixels) and acquisition rate of 123 Hz, Figure 2. A geometrical resolution of 0.067 mm/pixel was obtained by placing the thermocamera at 170 mm from the specimen and by using a 50 mm lens with a 12 mm extension ring. All specimens were pre-cracked to a crack length of 2.5 mm according to ASTM E-647.
A second infrared camera, Deltatherm 1560 by Stress Photonics, with an InSb photonic detector (320x256 pixels) on the opposite side of the specimen was used only to monitor the crack size according to Standard [3].

Figure 2. Experimental set-up used for testing

4. Methods and data analysis

Acquisition systems used in TSA are usually based on a correlation in frequency, amplitude and phase of the detected signal with a reference signal coming from the loading system [29]. As already stated, TSA provides a *S* signal proportional to the peak-to-peak variation in temperature during the peak-to-peak variation of the sum of principal stress. *S* is usually presented as a vector, where modulus is proportional to the change in temperature due to the thermoelastic effect and the phase φ means the angular shift between the thermoelastic and the reference signal [17].
In order to respect the adiabatic conditions, TSA is usually performed by applying a sinusoidal loading to material with a suitable loading frequency [29]. In this case, the generic measured uncalibrated thermographic signal *s* can be represented in the time domain as follows:

$$s = \frac{1}{A}\sigma_a \sin(\omega t + \pi + \varphi) = \frac{S}{2}\sin(\omega t + \pi + \varphi) \tag{3}$$

where ω is the frequency loading, σ_a is the stress semi-amplitude and φ is the phase angle between thermoelastic and loading signal.
Referring to equation (3), a mathematical algorithm has been used to extract pixel by pixel phase angle and the amplitude S of the thermoelastic signal. In particular, a suited signal model has been used, as indicated in equation (4):

$$s = b_1 + b_2 \sin(\omega t + \Psi) \tag{4}$$

where the term b_1 represents the mean temperature rise, $b_2=S/2$, and $\Psi=\pi+\varphi$.

4.1 SIF evaluation by means of amplitude of thermoelastic signal

The following important relationship can be used for the thermoelastic signal obtained from a point (r, θ) in a crack-tip stress field resulting from any combination of mode I and mode II loading [29]:

$$SA = \frac{2K_I}{\sqrt{2\pi r}}\cos(\theta/2) - \frac{2K_{II}}{\sqrt{2\pi r}}\sin(\theta/2) \tag{5}$$

Considering a series of signal line plots taken parallel to the line of the crack ($y=constant$), eq. (5) is developed by putting $K_{II}=0$ and by replacing r in the K_I term by $y/\sin\theta$.
Deriving eq. (5) with respect to θ:

$$\left(\frac{\partial S}{\partial \theta}\right) = \frac{K_I}{A\sqrt{2\pi y}}\left[\frac{\cos\left(\frac{\theta}{2}\right)\cos\theta}{\sqrt{\sin\theta}} - \sin\left(\frac{\theta}{2}\right)\sqrt{\sin\theta}\right] \tag{6}$$

it is simply observed that the partial derivative of S with respect to θ is zero when $\theta=60°$ and thus it follows that maximum signal ($Smax$) in a line plot taken parallel to the crack occurs at $\theta=60°$. By substituting this value of θ [29]:

$$y = \left(\frac{3\sqrt{3}\Delta K_I^2}{4\pi A^2}\right)\frac{1}{S_{\max}^2} \tag{7}$$

From eq. 7, it is evident how y and $1/S^2_{max}$ are linearly related and that, if the constant A is known, ΔK_I can be obtained directly from the gradient of a graph of y versus $1/S^2_{max}$.
In the same way, the analysis for mode I loading can be based on signal plots along lines perpendicular to the crack and ahead of the crack tip ($x=constant$), [29].

As an example, in Figure 3 the maximum signal S_{max} is plotted around the crack tip versus the vertical distance y from the crack tip growth direction. The angular coefficient of the best fit line of collected data provides the SIF value.

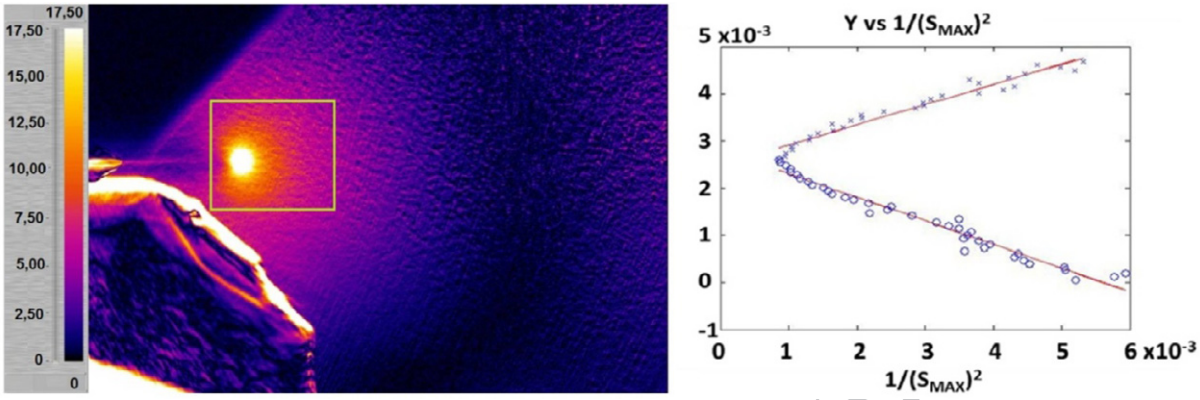

a b

Figure 3. Typical Amplitude signal map (a) and evaluation of the signal around the crack tip in the selected area (b) for AISI 422 at 80,000 cycles.

4.2 Crack growth evaluation by means of the phase of the thermoelastic signal

Phase angle depends on a number of parameters such as, for example, thickness of the painting or the grips of the loading machine. While phase can slightly change through the area analyzed due to non-perfect homogeneity of surface conditions, it remains locally constant in presence of linear elastic behaviour of material and steady state conditions. Phase can change:

1. in presence of viscoelastic or plastic behaviour of material [17], [22-25], [36]
2. in presence of high stress gradient leading to heat conduction in material and to the loss of adiabatic conditions [28].

In fracture mechanics, near the crack tip region, two phenomena that lead to a lack of adiabatic conditions occur: heat generation due to plastic work and the presence of high stress gradients [16-19]. These phenomena lead to a change in phase signal. By analyzing the phase image of the thermoelastic data, it is possible to evaluate the crack tip position. In Figure 4 (a), the typical phase map during a fracture mechanic test is shown.
Where adiabatic conditions were achieved, the phase signal should be constant; in fact thermoelastic and reference signal are set in phase. This condition is verified away from the crack tip where there are linear elastic conditions. Near the crack tip, adiabatic conditions were lost due to plasticity and high stress gradients [16-19]. The position of the crack tip can be extracted by plotting the phase values along a profile taken across the crack as shown in Figure 4.

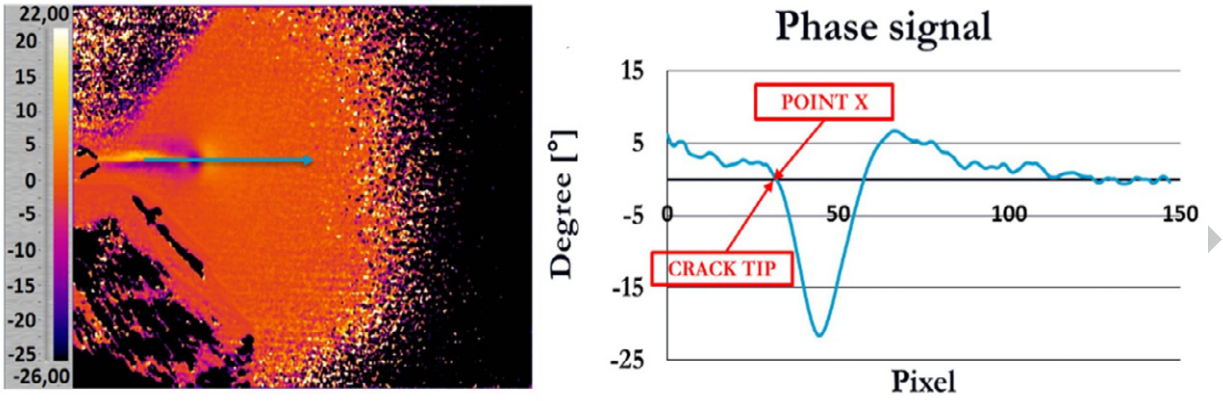

a b

Figure 4. Typical Phase Map (a) and Phase profile along crack tip (b) for AISI 422 at 80,000 cycles.

Considering Figure 4 (b), starting from the right, there is a region where the phase value is approximately constant and equal to zero. In all these points, adiabatic conditions are achieved. In proximity of the crack tip, there is a positive increment of the phase value that indicates a loss of adiabatic conditions due to plasticity and high stress gradients. Then the phase changes in value from positive to negative, which indicates the presence of a reverse plasticity (phase inverted compared to the first region). The phase value returns to zero (Point *X*) and then it starts to assume various values (positive and negative) because of the contact between the crack faces and the background reflection [19]. Point *X* can be adopted for the estimation of the crack tip position and for the evaluation of crack growth during the tests [15].

4.3 Proposed procedure for the rapid evaluation of Paris Law constants

During fatigue tests, a series of thermographic sequences were acquired with the infrared camera at constant regular intervals in the number of cycles by means of the Flir software RIR Max [37]. Amplitude and phase data were obtained for each sequence providing the data processing as described in the previous section (eq. 5) by means of IRTA™ by DES software [38].
In order to obtain the Paris Law constants with the proposed procedure, firstly, the calibration constant *A* (eq. 2) needed to be assessed. In this regard, in this work, a "dog-bone" specimen was used made of the same material used for tests. In this way, the calibration constant *A* can be assessed by measuring the average thermoelastic signal *S* on the gauge length area of the "dog-bone" specimen, Figure 5. Then, by knowing the stress field on the gauge length area of the specimen, the constant *A* is obtained by means of equation 1 [33].

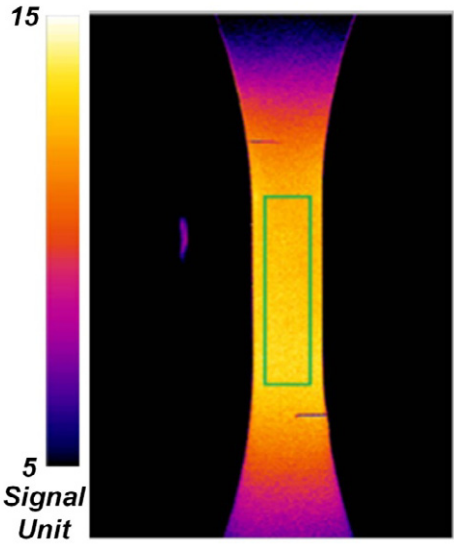

Figure 5. Amplitude signal map of a "dog-bone" specimen and area considered for the measuring of thermoelastic signal *S* (AISI 422 - $\Delta\sigma$ = 275 [MPa]).

Table 4 shows the values of the calibration constant *A* obtained for the four stainless steels tested with the stress amplitude used for "dog-bone" specimens. It should be noted how these values can be very different with respect to those obtained by other commercial systems due to the different algorithms used to obtain amplitude of the TSA signal.

Table 4. Calibration constant *A* and stress amplitude used for "dog-bone" specimens.

Material	$\Delta\sigma$ [MPa]	A [MPa/Signal Unit]
AISI 422	275	20.95
ASTM A182 grade F6NM	230	10.21
CF3M	120	24.54
CF8M	130	25.33

The proposed procedure can be summarized as follows:

1. Thermographic sequence acquisition with infrared camera;
   Thermal sequences of about 10 seconds have been acquired at 123 frames/s and at regular intervals of 2000 cycles during the test.

2. Thermoelastic phase and amplitude image assessing;
   About 2 minutes are required to extract the TSA data (phase and amplitude data) from each thermal sequence by means of the IRTA software.

3. Evaluation of the maximum value of thermoelastic signal *M(x,y)* from the amplitude image;
   This value represents the maximum stress amplitude reached in proximity of the crack tip.

4. Automatic detection of an analysis area (data matrix $[A]_{ixj}$) around the maximum value of thermoelastic signal;
   $[A]_{ixj}$ represents the area of interest for the following analysis and has dimensions i, j with $15< i<30$ and $15< j <30$ pixel (the min values of i, j were used during the first sequences on account of the presence of the test fixtures).

5. Automatic extraction of the analysis area (data matrix $[A]_{ixj}$) from the amplitude and phase images in order to obtain the amplitude data matrix $[S]_{ixj}$ and the phase data matrix $[\Phi]_{ixj}$;

6. Evaluation of the stress intensity factor ΔK_I from the amplitude data matrix $[S]_{ixj}$;
   The procedure described in section 4 has been used for evaluating ΔK_I.

7. Normalization of the selected phase area (data matrix $[\Phi]_{ixj}$) in order to report the average phase data to zero away from crack tip.
   Normalized area $[\Phi n]_{ixj}$ is obtained by subtracting the average value of phase signal of the selected area $[\Phi]_{ixj}$ ($[\Phi n]_{ixj} = [\Phi]_{ixj} - mean[\Phi]_{ixj}$);

8. Evaluation of the minimum value of phase signal $m(x,y)$ in the selected normalized area (data matrix $[\Phi n]_{ixj}$) and identification of the crack growth direction;
   The crack growth direction is obtained by joining the minimum value of phase signal and the crack tip position obtained at the end of the pre-crack procedure.

9. Plotting of the phase signal values along the crack growth direction;

10. Automatic assessment of the crack tip position in terms of coordinates x and y in the local reference system ($0, x,$ y) (local reference system of data matrix $([\Phi n]_{ixj})$;

11. Evaluation of the crack tip growth rate;
    Plotting of the crack tip position in the main reference system ($0, X, Y$) versus the number of cycles and using the incremental polynomial method for evaluating the crack growth rate [3];
    Automatic evaluation of the out-of-plane cracking limits [3].

12. Evaluation of the constants m and C by plotting da/dN $vs.$ ΔK_I.
    Accordingly, the Paris-Erdogan law is known:

$$\frac{da}{dN} = C(\Delta K_I)^m \tag{8}$$

The procedure is shown in Figure 6 in flow-chart form, and, in Figure 7 in graphic form. Matlab® code has been used for the processing of data from Step 3 to Step 12, but all routines can be easily adapted in equivalent open source software.

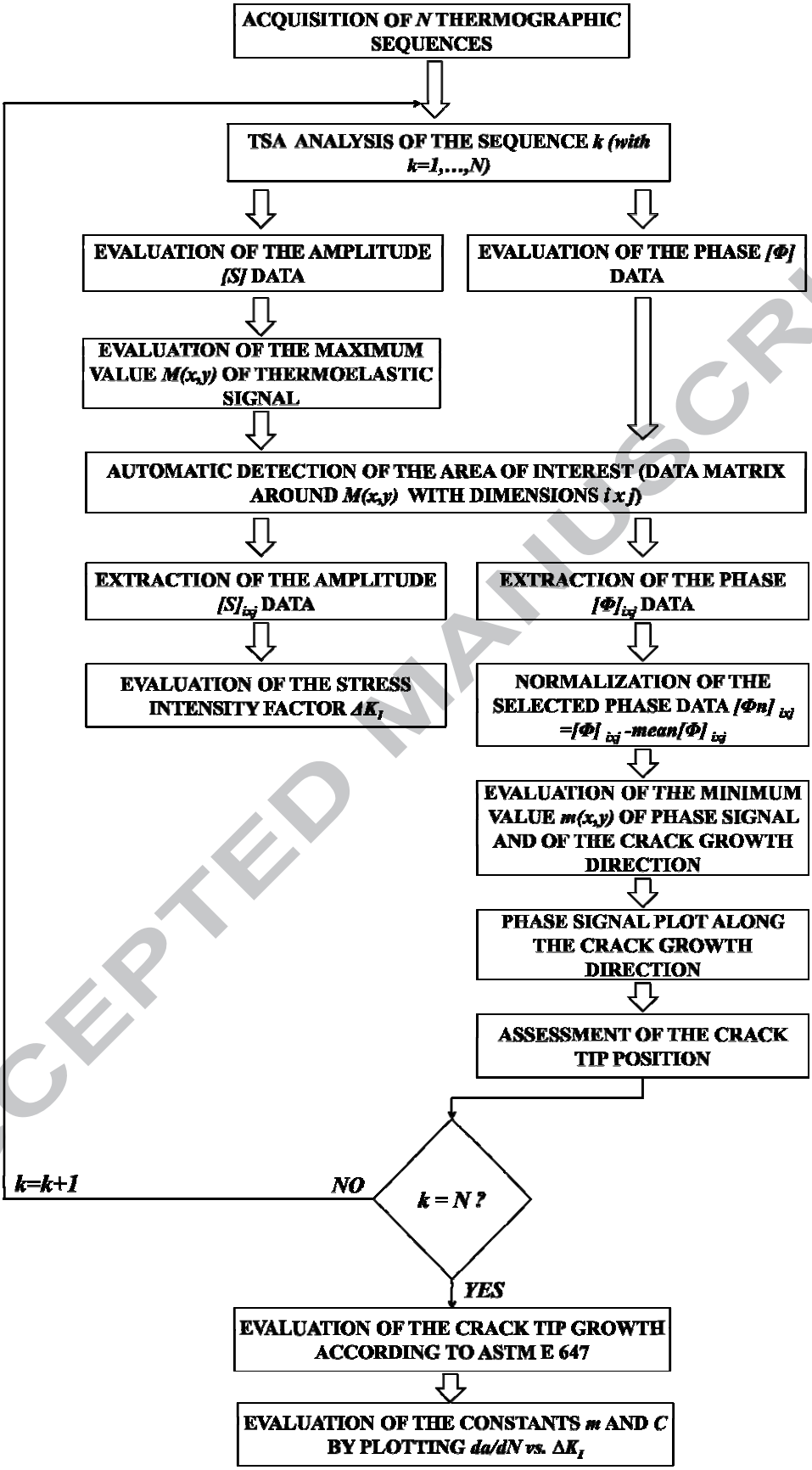

Figure 6. Flow chart of the proposed procedure for crack growth rate evaluation.

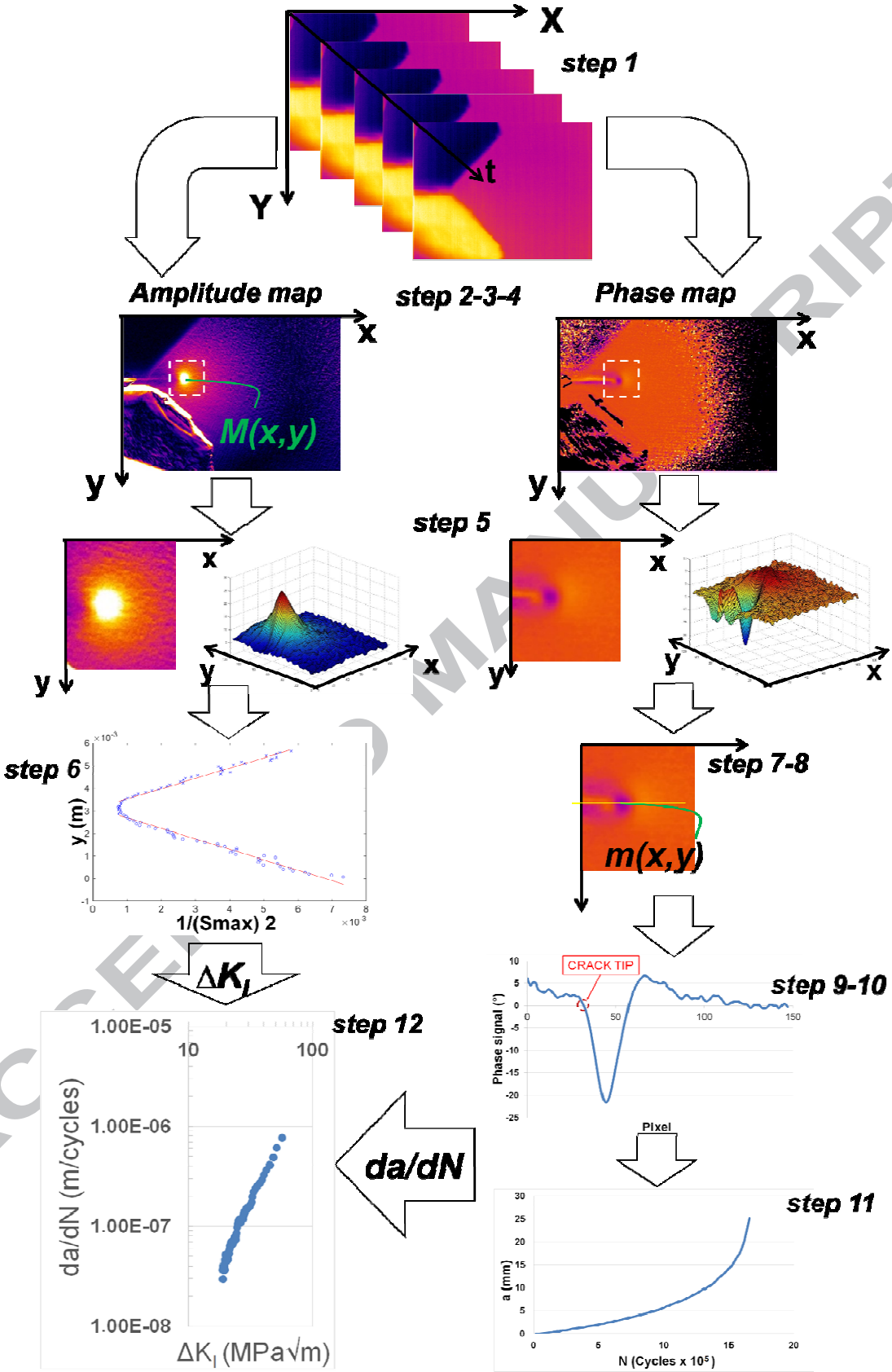

Figure 7. Graphical representation of proposed procedure

5. Results and discussion

In Figure 8, the phase maps and the phase data along the crack growth direction during the test are shown for AISI 422, Specimen 3. As illustrated in the previous section, these data are used to evaluate the crack length as the number of cycles increases.
For example, in Figure 8 (a), the crack length is of about 4 mm at 30,000 cycles. After 80,000 cycles, the crack grows to 8.5 mm (Figure 8 b) and in proximity of the failure (140,000 cycles) the crack reaches a length of about 19.5 mm (Figure 8 c).

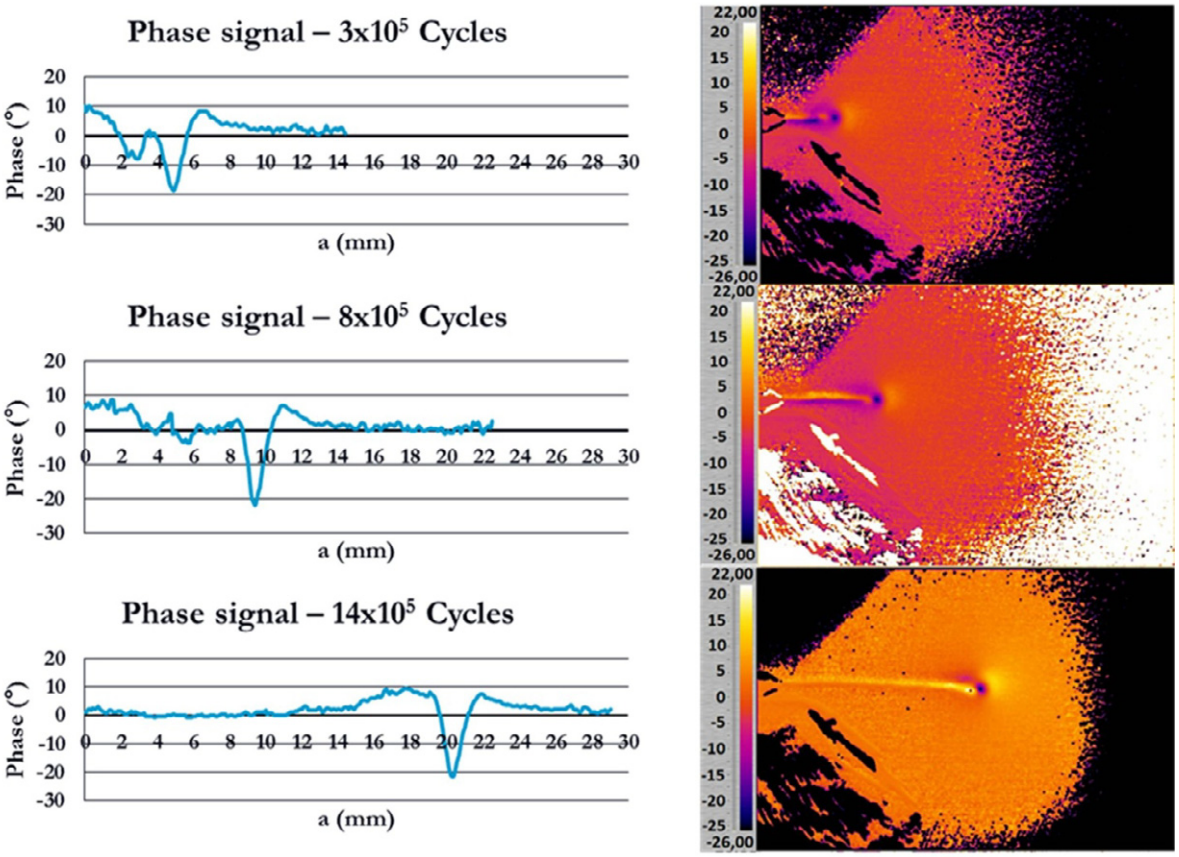

Figure 8. Phase map (right) and Phase profile along crack tip (left) at 30,000 cycles, 80,000 cycles and 140,000cycles for AISI 422 - Specimen 3.

In Figure 9, the crack tip growth trend is shown for Specimen 1 of each material as well as the fracture surfaces. Table 5 shows the constant load amplitude used for tests and the number of cycles performed until failure of specimens.
A comparison between the SIF values evaluated according to the Standard ASTM E 647 [3] and those obtained with the proposed procedure are shown in Figure 12 for Specimen 2 of the AISI 422.
In particular, ASTM E 647-00 provides the following equation for evaluating ΔK_I:

$$\Delta K_I = \frac{\Delta P}{B\sqrt{W}} \frac{(2+\beta)}{(1-\beta)^{3/2}} \left(0.886 + 4.64\beta - 13.32\beta^2 + 14.72\beta^3 - 5.6\beta^4\right) \quad (9)$$

where $\beta=a/W$, a is the crack length, B and W are two characteristic dimensions of specimen [3], in this case $B=12.5$ *mm* and $W=50$ *mm*.

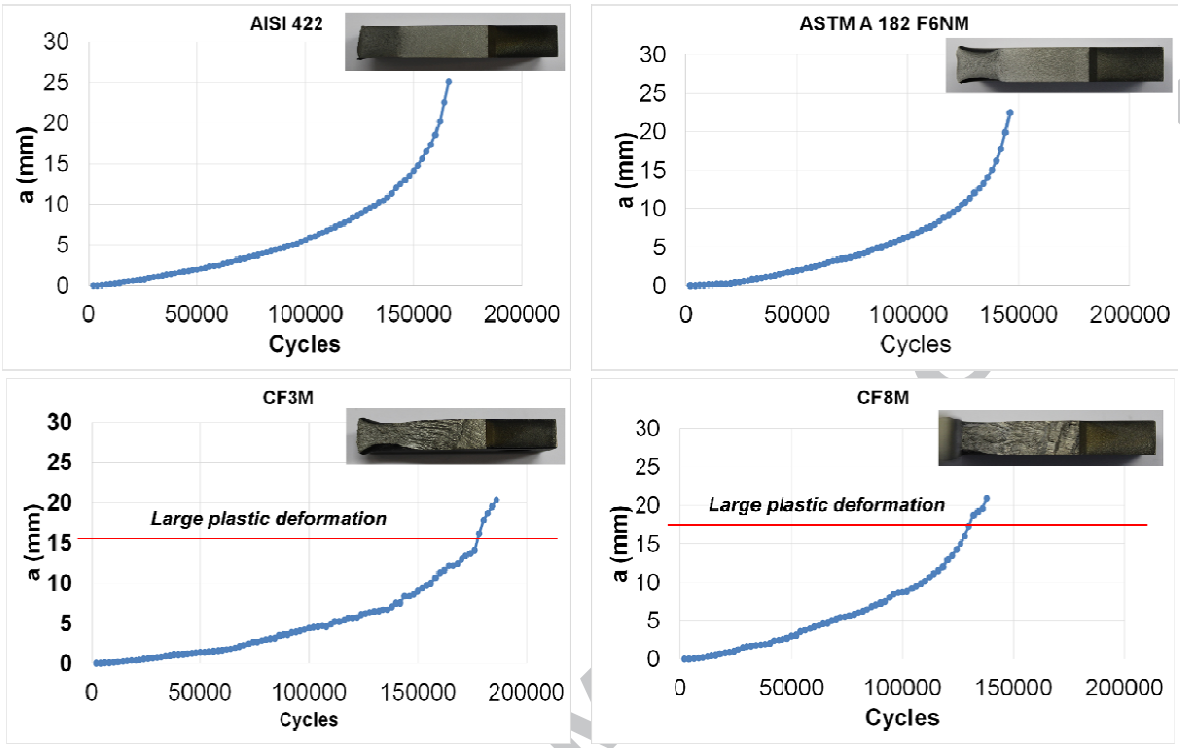

Figure 9. The crack tip growth trend for Specimen 1 of each material and fracture surfaces.

The differing fracture mechanics behaviour of both types of stainless steel used in this work (martensitic and austenitic steel) is clearly evident from Figures 9, 10 and 11.
The austenitic steel (CF3M and CF8M specimens) in the last 10,000 cycles presents a more ductile behaviour compared to the martensitic. This behaviour produces considerable plastic deformation before the final failure and a downward movement of the crack tip with respect to the main reference system (0, X, Y), Figure 10.

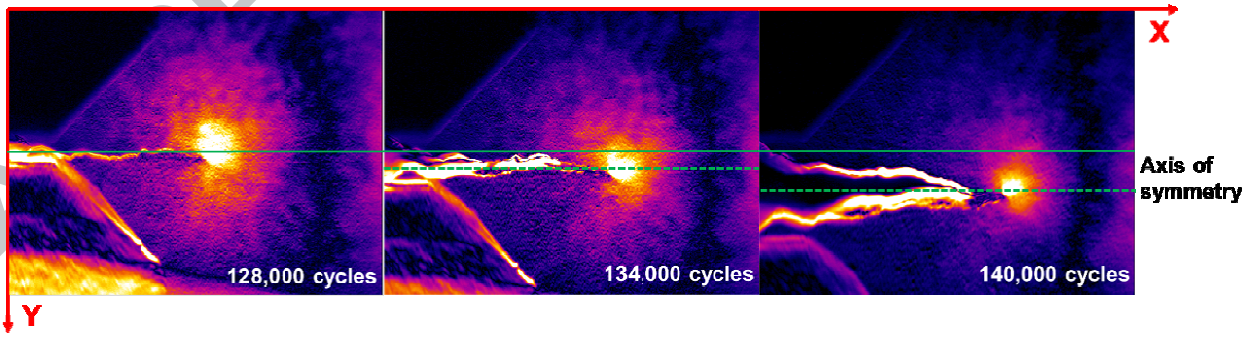

Figure 10. CF8M - Specimen 1, amplitude image at 128,000, 134,000 and 140,000 cycles.

In Figure 11 a) the envelope of the crack tip position is shown for both stainless steels, AISI 422 and CF8M. For the latter, the dotted line represents the crack tip envelope obtained with the proposed algorithm. The effect of the rigid downward motion due to the characteristic behaviour of

the material is clearly evident. In this case, a post-processing procedure was necessary in order to compensate the crack tip position along the coordinate Y. In Figure 11 b), the crack tip profile obtained with the proposed procedure (continuous red lines) is compared with the profile of the fracture surface. The two profiles are practically superimposable.

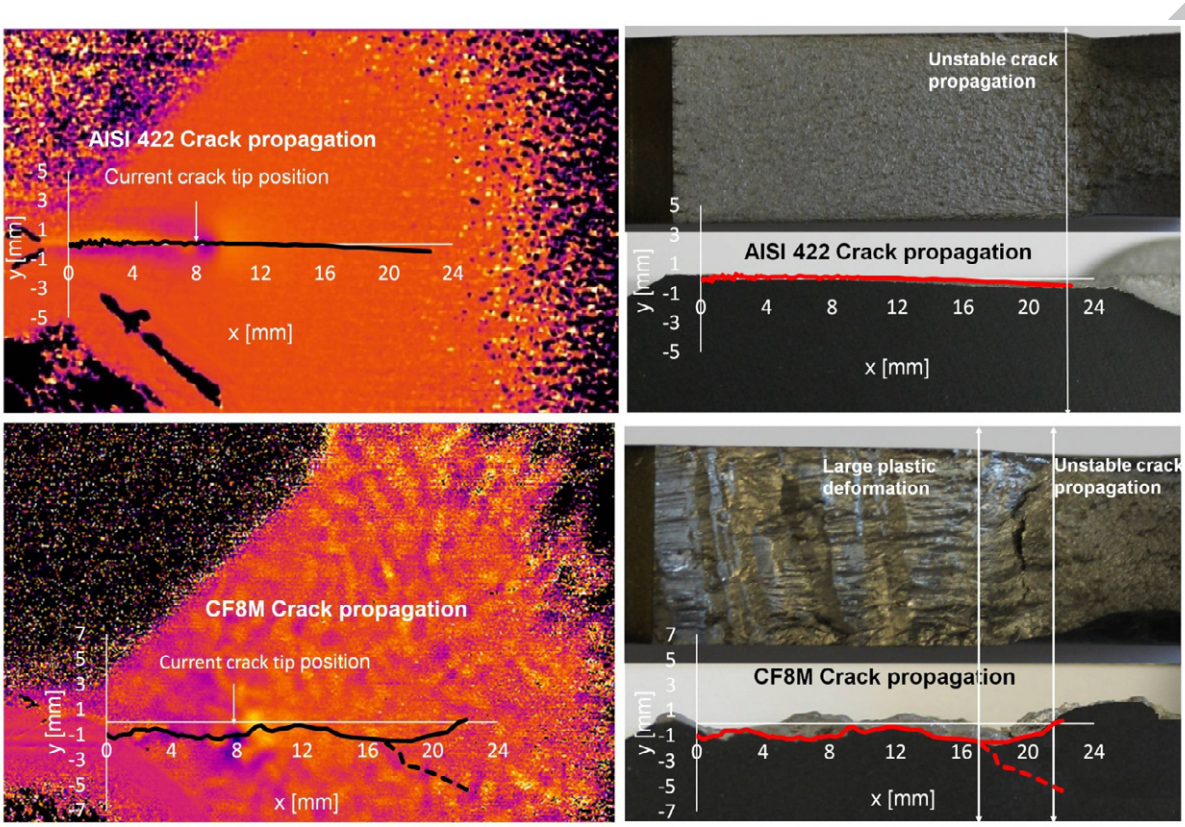

Figure 11. Crack propagation for martensitic (above, AISI 422 - Specimen 1 – 90,000 Cycles) and austenitic (below, CF8M - Specimen 1 – 100,000 Cycles) stainless steel by means of TSA technique on the left and real crack propagation surface on the right.

Table 5. Loads and number of cycles performed for all materials

Material/Specimen	ΔP [kN]	Cycles
AISI 422		
1	10.8	166,000
2	10.8	124,000
3	10.8	134,000
ASTM A182 grade F6NM		
1	12.4	146,000
2	12.4	142,000
3	12.4	138,000
CF3M		
1	9.9	186,000
2	9.9	164,000
3	9.9	214,000

CF8M		
1	9.45	138,000
2	9.45	198,000
3	9.45	164,000

Figure 12 illustrates how the proposed procedure provides ΔK_I values in good agreement with Standard ASTM.

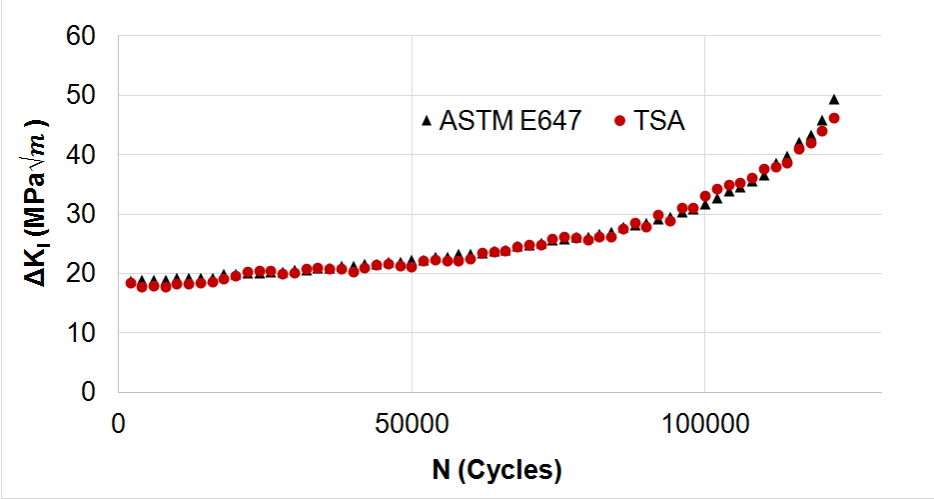

Figure 12. Comparison between the SIF values evaluated according to Standard ASTM E 647-00 and those obtained with the proposed procedure, (AISI 422 - Specimen 2).

Figures 13 and 14 summarize the data for both martensitic and austenitic steels respectively. In each graph, the results obtained from each specimen are reported in order to show the good repeatability of data. The coefficients of the Paris Law were evaluated considering the data deriving from the three specimens all together. In Table 6, the results obtained by performing the linear fitting of data shown in Figures 13 and 14 are reported. These are in good agreement with indications in literature [39], [40] for both martensitic and austenitic stainless steels. In particular, AISI 422 and ASTM A182 grade F6NM have a similar Paris equation and present a lower crack growth rate with respect to CF3M and CF8M.

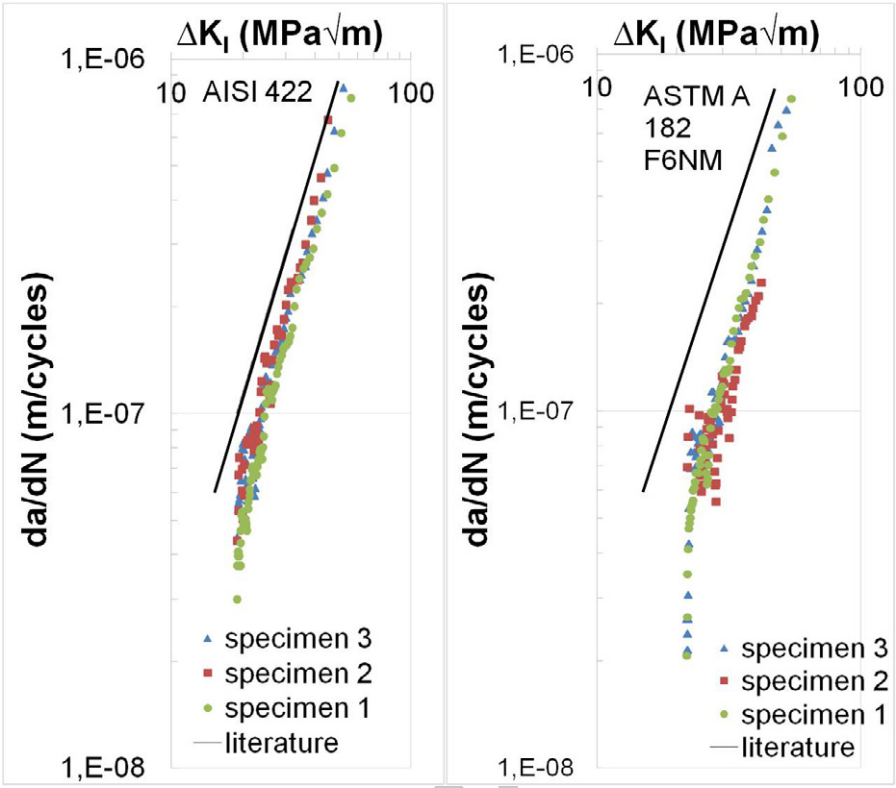

Figure 13. Crack growth rate obtained for martensitic stainless steels (AISI 422 and ASTM A182 grade F6NM) and comparison with literature.

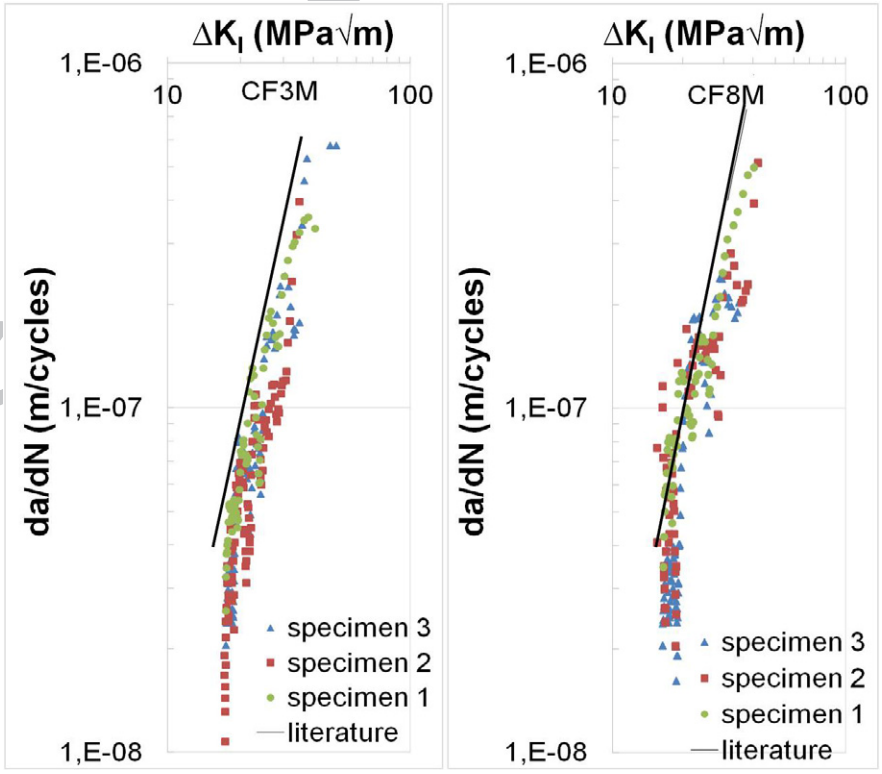

Figure 14. Crack growth rate obtained for austenitic stainless steels (CF3M and CF8M) and comparison with literature.

Table 6. Paris Law coefficients *m* and *C* obtained for all materials

Materials	m	C (m/cycles)
ASTM A 182 F6NM	2.56	1.90E-11
AISI 422	2.66	2.02E-11
CF3M	3.01	5.99E-12
CF8M	3.37	2.66E-12

Literature value for martensitic stainless steels class: m=2.25, C=1.67E-10 [m/cycles], [39]; m=2.25, C=1.36E-10 [m/cycles], [40].
Literature value for austenitic stainless steels class: m=3.25, C=7.62E-12 [m/cycles], [39]; m=3.25, C=5.61E-12 [m/cycles], [40].

6. Conclusions

In this work, a new procedure based on the Thermoelastic Stress Analysis (TSA) technique has been proposed for the monitoring of crack tip growth during fracture mechanics tests continuously and automatically.
Two martensitic (AISI 422 and ASTM A182 grade F6NM) and two austenitic (CF3M and CF8M) stainless steels were investigated by testing three CT specimens for each material. A cooled infrared camera has been used in order to acquire thermographic sequences during tests at regular intervals (2,000 cycles each).
The proposed procedure uses the TSA technique to extract the amplitude and phase data form thermal sequences in a simultaneous manner. These data are used to obtain respectively the SIF values and the crack growth rate in order to finally obtain the Paris Law constants.
Results are in good agreement with those obtained by Standards and reported in literature. In particular, AISI 422 and ASTM A182 grade F6NM have a similar Paris equation and present a lower crack growth rate with respect to CF3M and CF8M.
Main advantages when compared to traditional techniques are: a simple specimen preparation, a simple set-up, the on-line monitoring of the crack growth rate and an automatable procedure.
Finally, the proposed method can also be used for the monitoring of damage or crack growth within real and more complex structures subjected to actual loading conditions.

Acknowledgements

This work is part of a large-scale research project (PON-SMATI) aimed at identifying innovative steels for turbo machinery used in extreme environmental conditions. The authors would like to thank GE oil & gas (Nuovo Pignone S.r.l.) for the support and collaboration provided in the experimental tests.

References

[1] Paris P, Erdogan F. A critical analysis of crack propagation laws. Journal of Basic Engineering, Transactions of the American Society of Mechanical Engineers, 1963; D 85(4): 528-7, DOI: 10.1115/1.3656900.

[2] Ritchie RO. Mechanisms of fatigue-crack propagation in ductile and brittle solids. International Journal of Fracture 1999; 100:55-29.
[3] ASTM E 647-00: Standard Test Method for Measurement of Fatigue Crack Growth Rates, 2004.
[4] Réthore J, Limodin N, Buffière JY, Roux S, Hild F. Three-dimensional analysis of fatigue crack propagation using X-Ray tomography, digital volume correlation and extended finite element simulations. Procedia IUTAM 4 2012; 4:151-8.
[5] Saka M, Sato I, Abè H. NDE of a 3-D surface crack using magnetic field induced by DC current flow. NDT&E International 1998; 5:325-4.
[6] Williams JJ, Yazzie KE, Padilla E, Chawla N, Xiao X, De Carlo F. Understanding fatigue crack growth in aluminium alloys by *in situ* X-ray synchrotron tomography. International Journal of Fatigue 2013; 57:79-7.
[7] Kainuma S, Ahn JH, Jeong YS, Takahashi H. Evaluation on estimation in characteristics of fatigue crack using micro-encapsulated dye mixing paint. Engineering Failure Analysis 2015; 25:1-12.
[8] Tanabe H, Kida K, Takamatsu T, Itoh N, Santos EC. Observation of Magnetic Flux Density Distribution around Fatigue Crack and Application to Non-Destructive Evaluation of Stress Intensity Factor. Procedia Engineering 2011; 10:881-7.
[9] Cui ZQ, Yang HW, Wang WX, Yan ZF, Ma ZZ, Xu BS, Xu HY. Research on fatigue crack growth beahavior of AZ31B magnesium alloy electron beam welded joints based on temperature distribution around the crack tip. Engineering Fracture Mechanics 2015; 133:14-10.
[10] Yates JR, Zanganeh M, Tai YH. Quantifying crack tip displacement fields with DIC. Engineering Fracture Mechanics 2010; 77:2063-14.
[11] Carrascal I, Casado JA, Diego S, Lacalle R, Cicero S, Álvarez JA. Determination of the Paris' law constants by means of infrared thermographic techniques. Polymer Testing 2014; 40:39-7.
[12] Guduru PR, Zehnder AT, Rosakis AJ, Ravichandran G. Dynamic full field measurements of crack tip temperatures. Engineering Fracture Mechanics 2001; 68:1535-22.
[13] Fedorova AYU, Bannikov MV, Plekhov OA, Plekhova EV. Infrared thermography study of the fatigue crack propagation. Frattura ed Integrità Strutturale 2012; 21:46-8.
[14] Tomlinson RA, Olden EJ. Thermoelasticity for the analysis of crack tip stress fields – a review. Strain 1999; 35:49-7.
[15] Tomlinson RA, Patterson EA. Examination of Crack Tip Plasticity Using Thermoelastic Stress Analysis. Thermomechanics and Infra-Red Imaging. In: Proceedings of the Society for Experimental Mechanics Series 2011; Volume 7, pp 123-7.
[16] Diaz FA, Patterson EA, Tomlinson RA, Yates RA. Measuring stress intensity factors during fatigue crack growth using thermoelasticity. Fracture of Engineering Materials and Structures 2004; 27(7):571–13.
[17] Diaz FA, Patterson EA, Yates RA. Some improvements in the analysis of fatigue cracks using thermoelasticity. International Journal of Fatigue 2004; 26(4):365–12.
[18] Diaz FA, Patterson EA, Yates RA. Application of thermoelastic stress analysis for the experimental evaluation of the effective stress intensity factor. Frattura ed Integrità Strutturale 2013; 25:109-8.

[19] Diaz FA, Patterson EA,Yates RA. Differential Thermography Reveals Crack Tip Behaviour?. In: Proc. 2005 SEM Annual Conf. on Exp. App. Mech., Society for Experimental Mechanics, 2005, pp. 1413-6.
[20] Ancona F, De Finis R, Palumbo D, Galietti U. Crack growth monitoring in stainless steels by means of TSA technique. Procedia Engineering 2015; 109:89-8.
[21] Palumbo D, Ancona F, De Finis R, Galietti U. Experimental study of the crack growth in stainless steels using thermal methods. Procedia Engineering 2015; 109:338-8.
[22] Palumbo D, Galietti U. Characterization Of Steel Welded Joints By Infrared Thermographic Methods. Quantitative Infrared Thermography Journal 2014; 11:42-11.
[23] Galietti U, Palumbo D. Application of thermal methods for characterization of steel welded joints. 14th International Conference on Experimental Mechanics, ICEM 2014; Poitiers; France; 4-9 July 2010. EPJ Web of Conferences, Volume 6, Article number 38012.
[24] Galietti U, Palumbo D, De Finis R, Ancona F. Fatigue Damage Evaluation of Martensitic Stainless Steel by Means of Thermal Methods. In: National Conference IGF XXII, 1-3 July, Rome, 2013, pp 80-11.
[25] Galietti U, Palumbo D, De Finis R, Ancona F. Fatigue limit evaluation of martensitic steels with thermal methods. In: QIRT Conference, 7-11 July, Bordeaux, 2014.
[26] Dulieu-Barton JM. Introduction to thermoelastic stress analysis. Strain 1999; 35:35–5.
[27] Pitarresi G, Patterson EA. A review of the general theory of thermoelastic stress analysis. The Journal of Strain Analysis for Engineering Design 2003; 38(5):405–13.
[28] Wang WJ, Dulieu-Barton JM, Li Q. Assessment of non-adiabatic behaviour in thermoelastic stress analysis of small scale components. Experimental Mechanics 2010; 50:449–13.
[29] Harwood N, Cummings WM, Thermoelastic Stress Analysis, Adam Hilger, Bristol Philadelphia and New York, 1991.
[30] Palumbo D, Galietti U. Data Correction for Thermoelastic Stress Analysis on Titanium Components. Experimental Mechanics 2016; 56(3):451-12.
[31] Stanley P. Applications and potential of thermoelastic stress analysis. Journal of Materials Processing Technology 1997; 64:359-12.
[32] Dunn SA. Using Nonlinearities for Improved Stress Analysis by Thermoelastic Techniques. Appl. Mech. Rev. 1997; 50(9):499-15.
[33] Dulieu-Smith SM. Alternative calibration techniques for quantitative thermoelastic stress analysis. Strain 1995; 31:9-8.
[34] McGuire MF. Martensitic Stainless Steels. Stainless Steels for Design Engineers. Asm International. 2008, pp. 123-135, ISBN: 978-0-87170-717-8.
[35] Tomei R. Criteri di scelta degli acciai inossidabili in funzione degli impieghi. La meccanica italiana. 1981; 147.
[36] Connesson N, Maquin F, Pierron F. Experimental Energy Balance During the First Cycles of Cyclically Loaded Specimens Under the Conventional Yield Stress. Experimental Mechanics 2011; 51:23-22.
[37] ResearchIR Max (RIR Max), (2015). FLIR System, Inc. Wilsonville, USA.
[38] IRTA™ Manual, (2015). Diagnostic Engineering Solutions (DES srl).
[39] Damage Tolerance Assessment Handbook, Volume I: Introduction, Fracture Mechanics, Fatigue Crack Propagation. U.S. Department of Transportation, Research and Special Programs Administration, Volpe National Transportation System Center, Kendall Square, Cambridge, October 1993.

[40] Vergani L. Meccanica dei materiali, McGraw Hill, Milano, 2001, ISBN:88 386 0860-1.

ΔT temperature increment $= T - T_0$

K thermoelastic constant

σ_1, σ_2 principal stresses

α coefficient of thermal expansion

ρ density of the material

Cp specific heat at constant pressure

A thermoelastic calibration factor

S infrared camera output signal

$\Delta\sigma$ stress amplitude

σ_a stress semi-amplitude = $\Delta\sigma/2$

ω frequency of loading

φ phase angle between thermoelastic signal and loading

b_1 mean temperature rise

K_I stress intensity factor (mode I)

K_{II} stress intensity factor (mode II)

r, θ polar coordinates measured from the crack tip

y coordinate parallel to the line of the crack

S_{max} maximum thermoelastic signal

N number of cycles

da/dN crack growth rate

C, m Paris Law constants

ΔP loading amplitude

B, W characteristic dimensions of specimens according to Standard

a crack length

$M(x,y)$ maximum value of thermoelastic signal

$[A]_{ixj}$ analysis area around the maximum value (M(x,y))

$[S]_{ixj}$ amplitude data matrix of thermoelastic signal

$[\Phi]_{ixj}$ phase data matrix of thermoelastic signal

$[\Phi n]_{ixj}$ normalized phase data matrix of the thermoelastic signal

$m(x,y)$ minimum value of phase signal